

# **Spatially anisotropic Kondo resonance intertwined with superconducting gap in kagome metal $\text{CsV}_{3-x}\text{Cr}_x\text{Sb}_5$**

Zichen Huang<sup>1,2#</sup>, Hui Chen<sup>1,2,3#✉</sup>, Zhongqin Zhang<sup>4#</sup>, Hao Zhang<sup>1,2#</sup>, Zhen Zhao<sup>1,2</sup>, Ruwen Wang<sup>1,2</sup>,  
Haitao Yang<sup>1,2,3</sup>, Wei Ji<sup>4✉</sup>, Ziqiang Wang<sup>5</sup>, and Hong-Jun Gao<sup>1,2,3✉</sup>

<sup>1</sup>*Beijing National Center for Condensed Matter Physics and Institute of Physics, Chinese Academy of Sciences, Beijing 100190, PR China*

<sup>2</sup>*School of Physical Sciences, University of Chinese Academy of Sciences, Beijing 100190, PR China*

<sup>3</sup>*Hefei National Laboratory, 230088 Hefei, Anhui, PR China*

<sup>4</sup>*Beijing Key Laboratory of Optoelectronic Functional Materials & Micro-Nano Devices, Department of Physics, Renmin University of China, 100872, Beijing, China*

<sup>5</sup>*Department of Physics, Boston College, Chestnut Hill, MA 02467, USA*

<sup>#</sup>These authors contributed equally to this work

✉Correspondence to: [hjgao@iphy.ac.cn](mailto:hjgao@iphy.ac.cn); [wji@ruc.edu.cn](mailto:wji@ruc.edu.cn); [hchenn04@iphy.ac.cn](mailto:hchenn04@iphy.ac.cn)

The newly-discovered chromium-based kagome metal  $\text{CsCr}_3\text{Sb}_5$  has garnered significant interest due to its strong electron correlations, intertwined orders and potential for unconventional superconductivity under high pressure. However, the nature of superconducting and magnetic interactions during the transition from the parent compound  $\text{CsV}_3\text{Sb}_5$  to  $\text{CsCr}_3\text{Sb}_5$  remains elusive. Here, we report the discovery of spatially anisotropic Kondo resonance which intertwines with the superconducting gap, facilitated by the introduction of magnetic Cr impurities into the kagome superconductor  $\text{CsV}_3\text{Sb}_5$ . In addition to the gradual suppression of long-ranged charge-density-wave orders, dilute Cr dopants induce local magnetic moments, giving rise to the emergence of Kondo resonances. In addition, the Kondo resonance forms spatially anisotropic ripple-like structures around the Cr dopants, breaking all local mirror symmetries. This anisotropy arises from the antiferromagnetic coupling between itinerant electrons and the Cr-induced spin-up electrons. Remarkably, as the Kondo screening develops, the coherence peak and depth of superconducting gap with finite zero-energy conductance significantly enhances. It indicates that non-superconducting pairs at the Fermi surface in the parent compound participate in the Kondo effect, effectively screening the magnetic moments of Cr dopants while simultaneously enhancing the superfluid density. Our findings pave a unique pathway for exploring the interplay between superconductivity and local magnetic moments in kagome systems.

The interplay between magnetism and superconductivity has been a central topic of condensed matter physics. While magnetism is believed to be detrimental for phonon mediated conventional superconductors, magnetic fluctuations on the other hand has been the pairing “glue” for multiple unconventional superconductors (USC). Antiferromagnetic (AFM) fluctuations are the most common driving force of superconductivity in cuprates, iron-based superconductors and heavy-fermion superconductors<sup>1,2</sup>, while ferromagnetic fluctuations has been associated with spin-triplet superconductivity, such as  $UTe_2$ <sup>3</sup>. Recently discovered vanadium-based kagome metal  $AV_3Sb_5$  ( $A = K, Rb, Cs$ ) have attracted continuous attention for been the first kagome material exhibiting superconductivity<sup>4,5</sup>.  $AV_3Sb_5$  possess cascade of exotic phenomena such as multiple Van Hove singularity near the Fermi level<sup>6-9</sup>,  $Z_2$  nontrivial topology<sup>5,10</sup>, anomalous Hall effect<sup>11</sup>, pair density wave<sup>12-14</sup> and electronic nematicity<sup>15-17</sup>.  $AV_3Sb_5$  has V-shaped superconductive gap with sign-preserving multi-band superconductivity<sup>18</sup>, and the superconductivity in this class of material has been proved to be sensitive to external perturbation. Double-dome superconductivity and unconventional competing with CDW are observed upon pressure<sup>19</sup>. In addition, chemical doping on  $AV_3Sb_5$  provides another effective perturbation to tune the underlying electronic structure, leading to intriguing phase diagram for multiple intertwined instabilities such as hole doping effect by substituting V with Ti<sup>20,21</sup> and isovalent doping by substituting V with Ta or Nb<sup>22,23</sup> have been reported. However, the doping-induced magnetism in kagome superconductors, however, was rarely explored.

Substituting V with magnetic Cr is expected to introduce magnetism into  $CsV_3Sb_5$ <sup>24-27</sup>. In addition, the chromium-based material  $CsCr_3Sb_5$ , having the same crystal structure of  $AV_3Sb_5$ , undergoes AFM phase transition under 55 K at ambient pressure, with increasing pressure, AFM order is suppressed and superconductivity emerge at 4.2 GPa near the quantum criticality point<sup>28-31</sup>. The multi-phase diagram of  $CsCr_3Sb_5$  resembles that of other USCs, and AFM fluctuations is proposed as pairing mechanism, positioning  $CsCr_3Sb_5$  as a potential USC candidate within kagome systems. Understanding the role of Cr in modulating magnetism and superconductivity in kagome superconductor  $CsV_3Sb_5$  is crucial to understanding the AFM order and pressure-induced superconductivity, but it remains elusive.

Here, we study the interaction between local magnetic moments and superconductivity in magnetic Cr-doped kagome superconductor  $CsV_{3-x}Cr_xSb_5$  by utilizing ultra-low temperature scanning tunneling microscope/spectroscopy (STM/STS). In addition to the gradual suppression of long-range CDW order, V dilute Cr doping induces Kondo resonances near the Fermi level, arising from the screening of local magnetic moments. The resonances propagate solely along one of the four equivalent directions, thus breaking all local mirror symmetries. Density functional theory (DFT) calculations attribute such anisotropic Kondo resonance to the antiferromagnetic coupling between itinerant electrons and the anisotropically distributed spin-up electrons induced by Cr-dopant moments. The V-Sb kagome lattice experiences strong magnetic frustration, leading to a ripple-like propagation of spin density, which contributes to the observed anisotropic resonance. Simultaneously, superconductivity evolves strikingly with Cr doping. In Kondo resonance phase, the coherence peak height and gap depth of superconducting gap significantly enhances, accompanied by unconventional spatial evolution of vortex bound states. Once the Kondo resonance disappears, the superconductivity is rapidly suppressed by magnetic ordering. These findings reveal a distinct superconducting phase in  $CsV_{3-x}Cr_xSb_5$ ,

providing new insight into the interplay between superconductivity and magnetism in kagome lattice metals.

We first investigate the topographic characteristics of Cr dopants in  $\text{CsV}_3\text{Sb}_5$ , achieved by substituting V atomic with Cr in the VSb kagome plane. The concentration of Cr dopants is described by  $x$  in the  $\text{CsV}_{3-x}\text{Cr}_x\text{Sb}_5$  (Fig. 1a). We have synthesized series of  $\text{CsV}_{3-x}\text{Cr}_x\text{Sb}_5$  with  $x$  ranging from 0 to 1.2 (Fig. 1b-d and Fig. S1). Compared with pristine sample, there are additional dumbbell-like topographic protrusions in the STM images of Sb terminated surfaces (Fig. 1h). The density of dumbbell-like protrusions increases simultaneously with the Cr concentrations (Fig. 1b-d). We thus attribute the dumbbell-like protrusions to the Cr dopants. The Cr dopants are embedded in the middle of two adjacent topmost Sb atoms, which results in the two-fold dumbbell-like protrusions located halfway between pairs of topmost Sb atoms (Fig. 1h). There are three equivalent two-fold axes of dumbbell-like protrusions, which correlates to three lattice directions (green shades in Fig. 1a).

We then study the evolution of CDW orders with Cr concentration by performing Fourier transforms (FT) of topographic images. In pristine  $\text{CsV}_3\text{Sb}_5$ , the long-ranged  $2 \times 2$  CDW ( $\mathbf{Q}_{3q-2a}$ ) and  $4a_0$  unidirectional charge order ( $\mathbf{Q}_{1q-4a}$ ) have been observed at the Sb surfaces<sup>12,32</sup>. For diluted doped sample ( $x = 0.012$ ), the Bragg peaks together with clear signature of  $\mathbf{Q}_{3q-2a}$  and  $\mathbf{Q}_{1q-4a}$  are observed (Fig. 1i). For the  $x=0.3$  sample, the intensity of CDW peaks become much weaker (Supplementary Fig. 1). Thus, we plot the FFT profile along high symmetry direction of samples, which shows that the peak intensity of both  $\mathbf{Q}_{3q-2a}$  and  $\mathbf{Q}_{1q-4a}$  gradually reduce with increasing Cr concentrations (Fig. 1j). The CDWs are nearly undetectable at a large concentration of  $x=1.2$ , which are consistent with previous transport works<sup>24,25,29</sup>.

Apart from the suppression of long-ranged charge orders, the dilute magnetic Cr dopants also introduce local magnetic moments. The local moments are screened by the surrounding itinerant electrons from non-magnetic metallic band of  $\text{CsV}_3\text{Sb}_5$ , which results in the Kondo resonance in the density of state<sup>33,34</sup>. The Kondo resonance exhibits a pronounced peak with asymmetric spectral shape near Fermi level in the representative  $dI/dV$  spectra obtained upon the Cr dopants of Cr-doped  $\text{CsV}_3\text{Sb}_5$  (i.e.  $x = 0.03$ , Fig. 2a). Such peak is absent from the  $dI/dV$  spectra of dopant free region. Except for the Kondo resonance peak at around -3 meV, there are no magnetic impurity states inside the superconducting gap, which reaches the strong coupling regime due to the Kondo screening of impurity magnetic moment<sup>35</sup>.

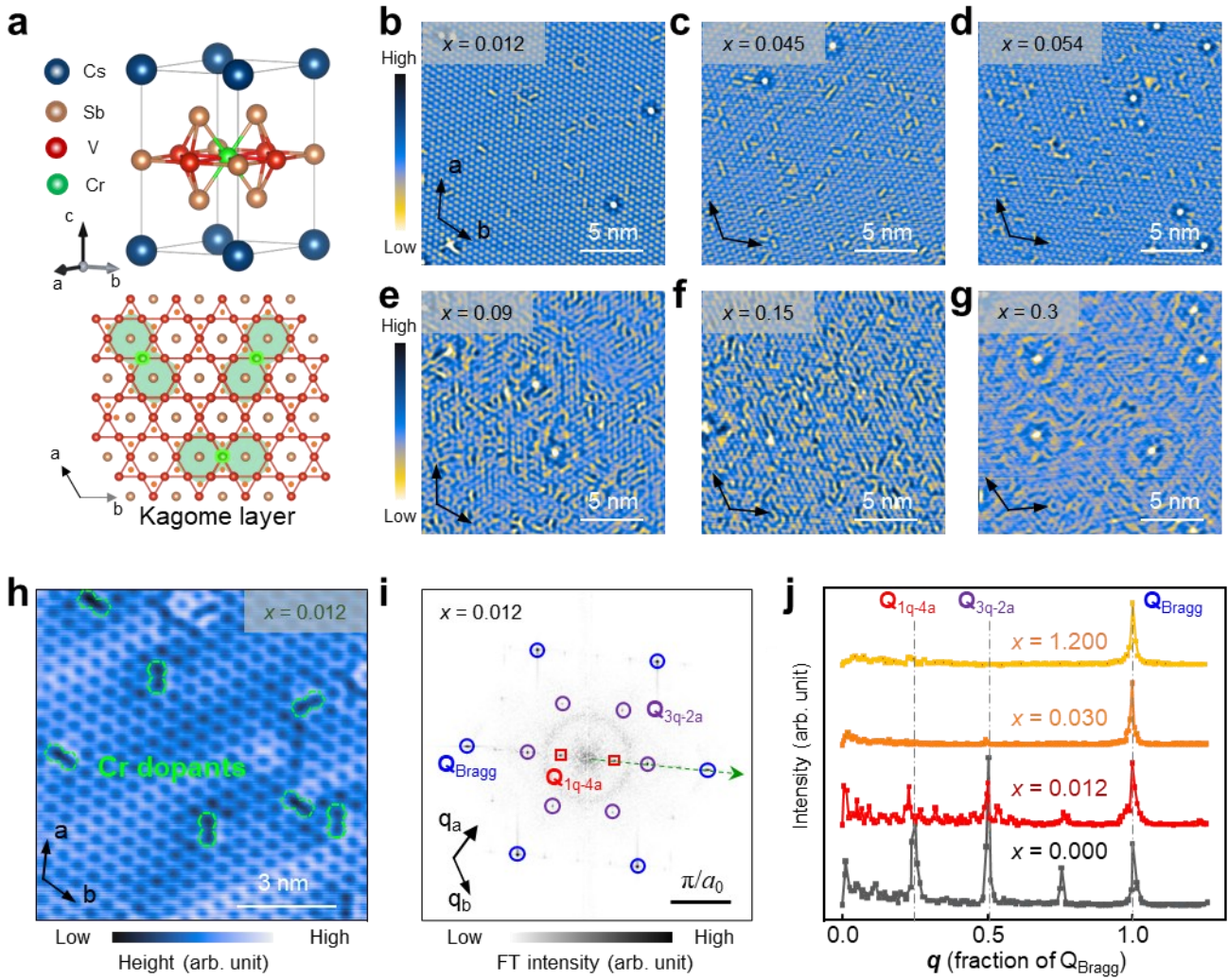


**Fig. 1. Atomic structures of  $\text{CsV}_{3-x}\text{Cr}_x\text{Sb}_5$  and evolution of CDWs with Cr concentrations.** **a**, Illustration of the  $\text{CsV}_{3-x}\text{Cr}_x\text{Sb}_5$  crystalline structure.  $\text{CsV}_{3-x}\text{Cr}_x\text{Sb}_5$  crystallizes in the parent  $\text{CsV}_3\text{Sb}_5$  structure (upper panel). The Cr atoms substitute V atoms in the VSb kagome plane (lower panel). **b-g**, STM images of Sb-terminated surface with different Cr concentrations  $x$ . (Sample bias:  $V_s = 100$  mV, setpoint:  $I_t = 1$  nA) **h**, Atomically-resolved STM image of Sb surface with Cr concentration  $x = 0.012$ , showing that Cr substitutions appear as two-fold protrusions marked by green dumbbells. ( $V_s = 100$  mV,  $I_t = 1$  nA) **i**, Fourier transform (FT) of STM topography with  $x = 0.012$ . The Bragg peaks  $\mathbf{Q}_{\text{Bragg}}$  are marked in blue circles. The vectors of  $2 \times 2$  CDW,  $\mathbf{Q}_{3q-2a}$  and  $4a_0$  unidirectional charge order  $\mathbf{Q}_{1q-4a}$  are marked in purple circles and red squares, respectively.  $V_s = 100$  mV,  $I_t = 1$  nA. **j**, Evolution of FT profile along high symmetry direction (black arrow in (i)) with Cr concentrations  $x$ . The bias of topography for the FT are  $V_s = -100$  mV.

To advance our understandings on the Kondo resonance, the typical  $dI/dV$  spectrum has been fitted to the Frota function<sup>36,37</sup>. By subtracting the  $dI/dV$  spectrum away from Cr dopants, the full width at half maximum (FWHM) of Kondo peak width fitted by Frota function is determined to be about 3.8 meV (Fig. 2b). The evolution of  $dI/dV$  spectra with external magnetic field perpendicular to the sample surface ( $B_z$ ) show the splitting of Kondo peak. With increasing  $B_z$ , the resonance peak first keeps nearly unchanged and start split into two peaks when  $|B_z| > 5$  T (Fig. 2c). Such evolution is clearer in the second derivative of the  $dI/dV$  spectra (Fig. 2d). The linear splitting of resonance peak corresponds to the Zeeman splitting of spin doublet for the local moment of Cr dopant. We describe the two split peaks with double Frota functions (Supplementary Fig. 3) and obtain the linear relationship between splitting energy  $\Delta$  and magnetic field with  $\Delta = 0.93 \mu_B B$  (Fig. 2e). The subtracting moment is close to the effective magnetic moment  $\mu_{\text{eff}} = 1.26 \pm 0.12 \mu_B$  per Cr atom<sup>30</sup>. An intuitive explanation is that the spin orientation of local moment around Cr dopant is parallel to the kagome plane, and strong out-of-plane magnetic field flop the spin from in-plane to out-of-plane direction, leading to the Zeeman splitting. Such phenomena is in consistent with Kondo effect in strong coupling regime<sup>35,38,39</sup>. We note that the energy of Kondo peaks could vary from -10 meV to 10 meV for different Cr dopants in the same surface region (Supplementary Fig. 2).

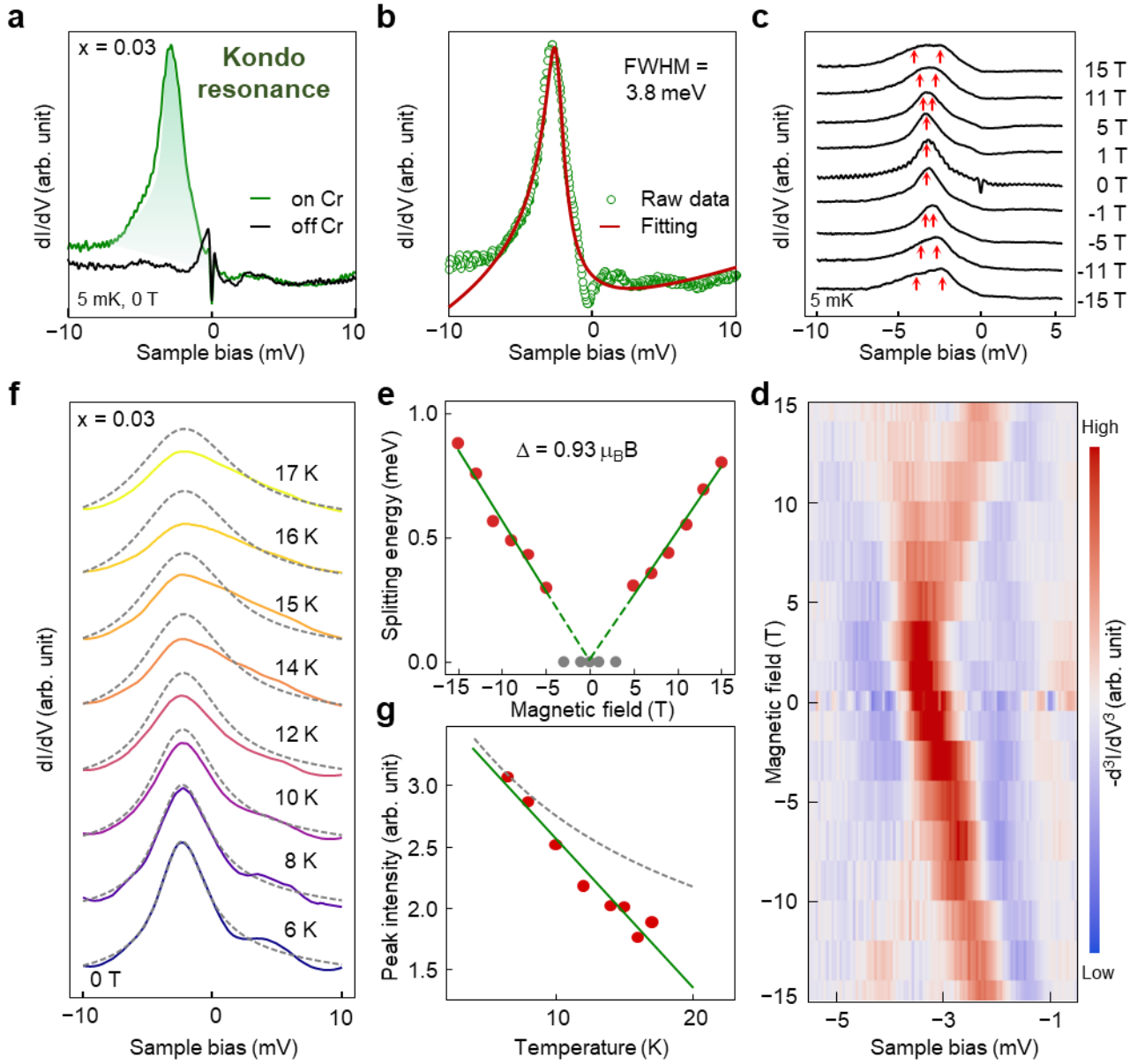


**Fig. 2. Field and temperature evolution of Kondo resonance on the Cr dopants of  $\text{CsV}_{3-x}\text{Cr}_x\text{Sb}_5$  ( $x=0.03$ ).** **a**,  $dI/dV$  spectra taken away from Cr dopant (black) and on the Cr dopant (green) ( $V_s = 10$  mV,  $I_t = 1$  nA,  $V_{\text{mod}} = 50$   $\mu\text{V}$ ,  $T_{\text{base}} = 5$  mK,  $x = 0.03$ ) showing a pronounced Kondo resonance peak on the Cr dopant. **b**, The  $dI/dV$  spectra subtracted with a linear background (green dot), showing that the Kondo peak can be fitted by Frota function (red curve), with a Full width at half maximum (FWHM) of  $\sim 3.8$  meV. **c,d** Magnetic field evolution of  $dI/dV$  spectra (**c**) and the second derivative curves (**d**) on Cr dopants, showing the Zeeman splitting of Kondo peak at field higher than 5 T ( $V_s = 10$  mV,  $I_t = 1$  nA,  $V_{\text{mod}} = 50$   $\mu\text{V}$ ,  $T_{\text{base}} = 5$  mK). **e**, Magnetic field dependence of the splitting  $\Delta$  (red dots) with linear fit (green line), yielding the relation  $\Delta = 0.93\mu_B B$ ,  $\Delta$  shows no sign of splitting with  $|B| < 5$  T and therefore is set to 0. **f**, Temperature dependence of the Kondo resonance with Cr concentrations  $x = 0.03$  ( $V_s = -10$  mV,  $I_t = 1$  nA,  $V_{\text{mod}} = 50$   $\mu\text{V}$ ), the evolution considers only the thermal broadening are indicated in dashed gray line, calculated with spectra in 6.47 K. **g**, Temperature dependence of the Kondo peak's intensity at -3 meV (red dots) derived by the spectra taken on the Cr dopant subtracted by the spectra taken away from the Cr dopant, a linear fit to the Kondo peak's intensity is shown in green line, the effect of thermal broadening calculated with spectra in 6.47 K is indicated by the dashed blue line.

To estimate the critical temperature of Kondo resonance, we also study the temperature evolution of  $dI/dV$  spectra for the same Cr dopant. As the temperature increases from 6 K to 17 K, the resonance peak broadens rapidly with increasing temperature (colored solid curves in Fig. 2f). Such resonance peaks at elevated temperatures are shallower than the numerically calculated spectra merely from the influence of Fermi-Dirac distribution based on that measured at 6.5 K (grey dashed curve in Fig. 2f). It indicates that the resonance peak becomes intrinsically suppressed with elevated temperature. A linear fit to the evolution of peak with temperature (Fig. 2g) shows the peak vanish at a critical temperature of about 21 K.

We next study the real-space distribution of Cr dopant induced Kondo resonance. In contrast to the symmetric real-space distribution of Kondo resonance in the previous reports<sup>40,41</sup>, the spatial distribution of Kondo resonance shows intriguingly symmetry-breaking ripple-like patterns surrounding the Cr dopant. In the STM topographic image obtained on the Sb surface of  $x = 0.012$  sample at large sample bias, i.e. 500 mV, the Cr dopants appear as symmetric two-fold dumbbells (Fig. 3a and Fig. 1h). When sample bias is set at around the Kondo peak, i.e. 5 mV, bright “ripples” propagating along one of the lattice directions appear around the dopant (Fig. 3b). The distance between each protrusion in the ripple equals to the lattice constant  $a_0$ .

The bright protrusions are located around the V-formed triangles in kagome structure, the Cr dopant lies the position between the first two bright protrusions. The spatial distribution of Kondo resonance is further demonstrated by the  $dI/dV$  linecut (Fig. 3c) along the stripe direction and a direction rotated by  $120^\circ$ , respectively. In addition, the  $dI/dV$  map at 5 meV (Fig. 3d), which is the energy position of the intensity peak, exhibit similar symmetry-breaking ripples with low-energy STM image. In contrast,  $dI/dV$  map at energy away from the Kondo resonance, i.e. -5 meV, shows opposite feature with that of 5 meV with stripe pattern formed by a reduction of LDOS (Fig. 3e). These observations demonstrate that the anisotropic stripe patterns are characteristic spatial distribution of Kondo resonance. Such anisotropic Kondo resonance is universal with respect to different Cr dopants (same spectra measurement to adjacent Cr dopant is shown in Supplementary Fig. 5). The anisotropic real-space distribution of Kondo resonance is observed on samples with different Cr concentrations, despite the variations of peak energy (Supplementary Fig. 6). The ripple direction is randomly aligned with one of the four equal lattice directions.

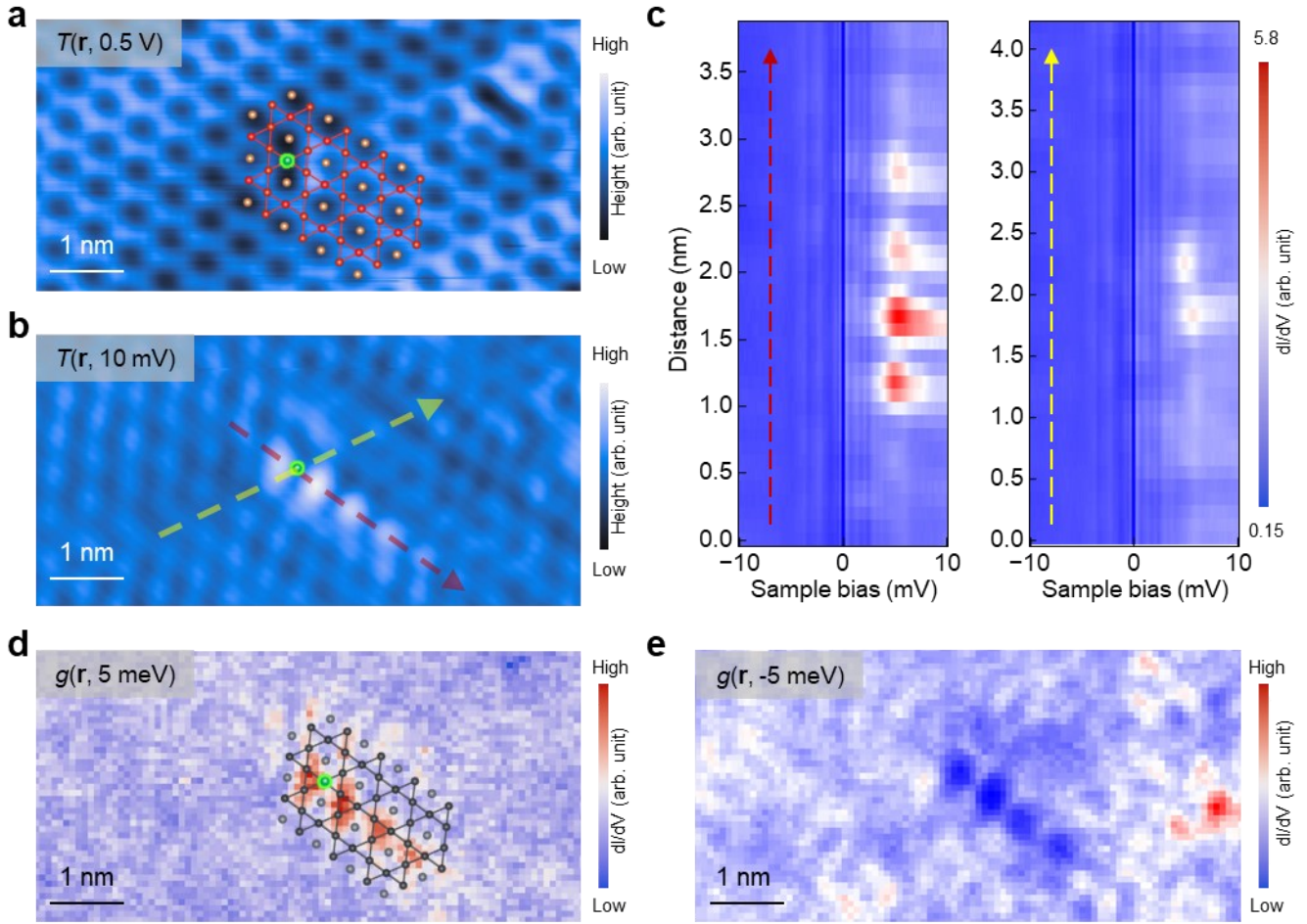


**Fig. 3. The anisotropic distribution of Kondo resonance in the real space.** **a,b**, Comparison of STM image of the same area with scanning bias of 500 mV (**a**) and 10 mV (**b**). A schematic model is overlaid in (**a**), showing that the direction of the bright protrusions in (**b**) is along a lattice direction. The distance between each protrusion equals to the lattice constant  $a_0$ . **c**, Color plot of  $dI/dV$  linecut across Cr dopant in directions parallel to  $a$  axis (red dashed arrow in (**b**)) and  $60^\circ$  to  $a$  axis (yellow dashed arrow in (**b**)) ( $V_s = 10$  mV,  $I_t = 1$  nA,  $V_{\text{mod}} = 50$   $\mu$ V,  $T_{\text{base}} = 5$  mK). **d,e**, LDOS map at 5 meV (**d**) and -5 meV (**e**), showing anisotropic ripple pattern around the Cr dopant ( $V_s = 10$  mV,  $I_t = 1$  nA,  $V_{\text{mod}} = 100$   $\mu$ V).

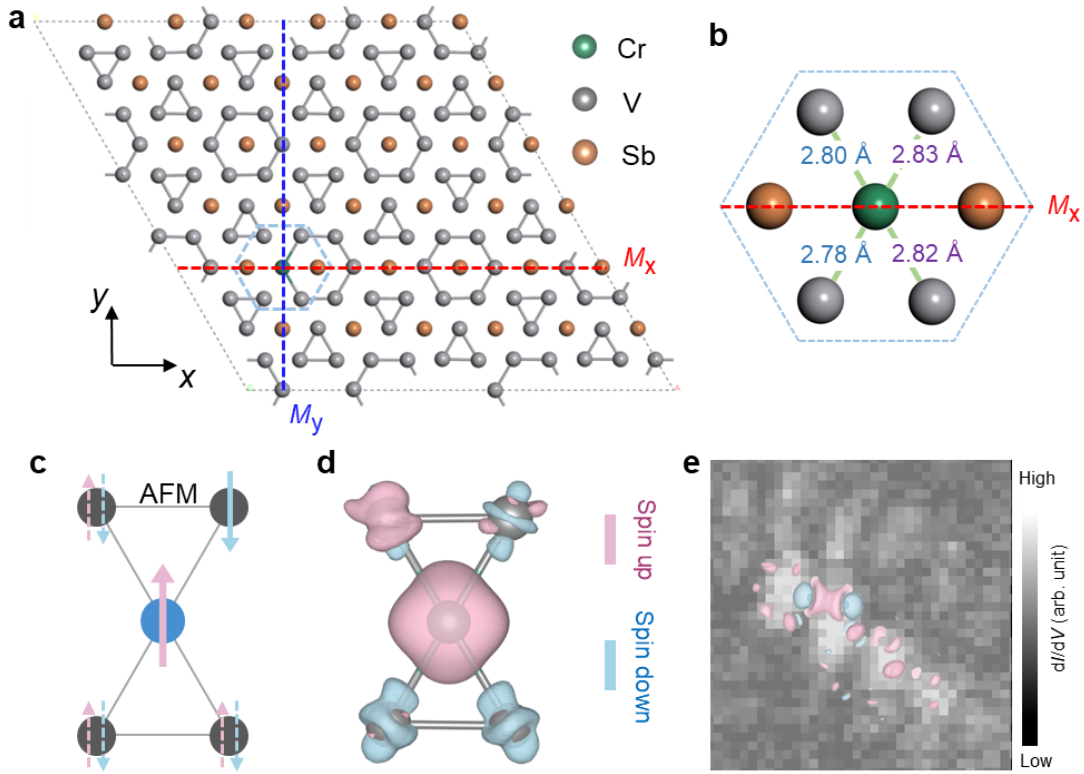


**Fig. 4. DFT calculations of spin density distribution around a Cr dopant in CsV<sub>3</sub>Sb<sub>5</sub>.** **a**, Fully relaxed atomic structure model of the V-Sb kagome layer after a V atom is substituted by a Cr atom. **b**, Zoom-in of the blue dashed region in **a**. Green dashed lines indicate Cr-V bonds, with bond lengths labeled. The blue and orange dashed lines in **a,b** represent the mirror planes for mirror symmetry operations  $M_x$  and  $M_y$ . If the system has  $M_x$  symmetry, two blue (or purple) bond lengths in **b** should be equal. **c**, Schematic of spin frustration in a di-triangle within a kagome lattice where the nearest neighboring sites are coupled antiferromagnetically. The blue (black) circle(s) denote the site(s) of the Cr dopant (adjacent V atoms). The violet up and cyan down arrows indicate up- and down-spins, respectively. The pairs of up and down dashed arrows indicate that the spin is undetermined at this site due to spin frustration. **d**, Isosurface contours of spin densities of Cr and its four neighboring V atoms for the most energetically favored magnet configuration as reveal by DFT. The color code follows the same scheme used in panel **c** (violet for spin-up and cyan for spin-down). An isosurface value of  $2 \times 10^{-3} e/\text{Bhor}^3$  was used for plotting. **e**, Experimental  $dI/dV$  mapping image acquired near a Cr dopant at a bias voltage of 5 meV, decorated with the theoretical surface spin density of the magnetic configuration presented in panel **d**, using the same color scheme in panels **c** and **d**, and an isosurface value of  $1.5 \times 10^{-4} e/\text{Bhor}^3$ .

The observed anisotropic Kondo resonance state may originate from either the Kondo screening process and the spatial distribution of Cr dopant-induced magnetic moments. Given the kagome-latticed V-Sb layer, where competing interactions induce magnetic frustration, the anisotropic spatial distribution of magnetic moments is the more plausible explanation. In contrast, the delocalized nature of conduction electrons typically favors isotropic screening. Our density functional theory calculations verify the anisotropic distribution of induced magnetic moments. The kagome-latticed V-Sb layer undergoes a CDW phase transition, where V atoms form alternating triangular and hexagonal arrangements that exhibit slightly different preference for Cr substitution. Specifically, Cr substitution at a hexagonal V site is energetically favored over substitution at a triangular site by 1.6 meV/Cr. The fully relaxed atomic structure of the V-Sb layer with a Cr dopant replacing a hexagonal V atom is shown in Fig. 4a. The presence of CDW-induced structural distortion breaks mirror symmetry  $M_y$ , which passes through the Cr atom and is parallel to the  $y$ - $z$  plane. Furthermore, Cr substitution introduces in-plane compressive strain, leading to asymmetric Cr-V bond lengths (see Fig. 4b), which, in turn, lifts an additional mirror symmetry  $M_x$  where the  $x$ - $z$  plane serves as the mirror plane. Additionally, the comparable lengths of these four Cr-V bonds implies that the Cr dopant can suppress the CDW order, which is consistent with experimental observations where the CDW signal disappears with an increase in Cr concentration (Fig. 1j).

The Cr dopant has one more  $d$  electron than an adjacent V atom, thereby introducing a local magnetic moment surrounded by non-local electrons from neighboring surface V atoms. Due to the magnetic proximity effect, the Cr local moment magnetizes adjacent V atoms through antiferromagnetic (AFM) couplings, leads to strong spin frustration within the kagome V-Sb layer (Fig. 4c). This frustration give rise to at least four candidate magnetic configurations (Supplementary Fig. 7d-g), each of which contains four AFM and two ferromagnetic (FM) nearest neighbor spin-exchange couplings within the corner-sharing bi-triangle unit show in Fig. 4c.

Our DFT calculations reveal that the magnetic configuration shown in Fig. 4d is the most stable among these configurations. Regardless of the initial magnetic configuration chosen from those shown in Supplementary Fig. 7d-g, the system invariably relaxes to the magnetic configuration illustrated in Fig. 4d, where one of the four nearest-neighboring V sites is polarized in alignment with the majority spin orientation (spin-up, in red) of the Cr dopant. The spin-up V and the Cr dopant form a line-like feature in the spin-up density, which extends along the Cr-V direction with gradually diminishing intensity, resulting in a quasi-one-dimensional ripple-like propagation pattern through the lattice (Supplementary Fig. 7h). This spin-density distribution in the Cr-V-Sb plane induces an anisotropic spin distribution on the Sb surface, as depicted in Supplementary Fig. 7i. These anisotropically distributed spin-up electrons undergo AFM coupling with itinerant electrons at low temperature, leading to the anisotropic Kondo resonance observed in our experiments. The spatial distribution of theoretically predicted majority spin density well aligns with the experimentally observed Kondo cloud, as illustrated by the striking agreement of the density supposing on the experimental  $dI/dV$  mapping acquired near the Fermi level in Fig. 4e.

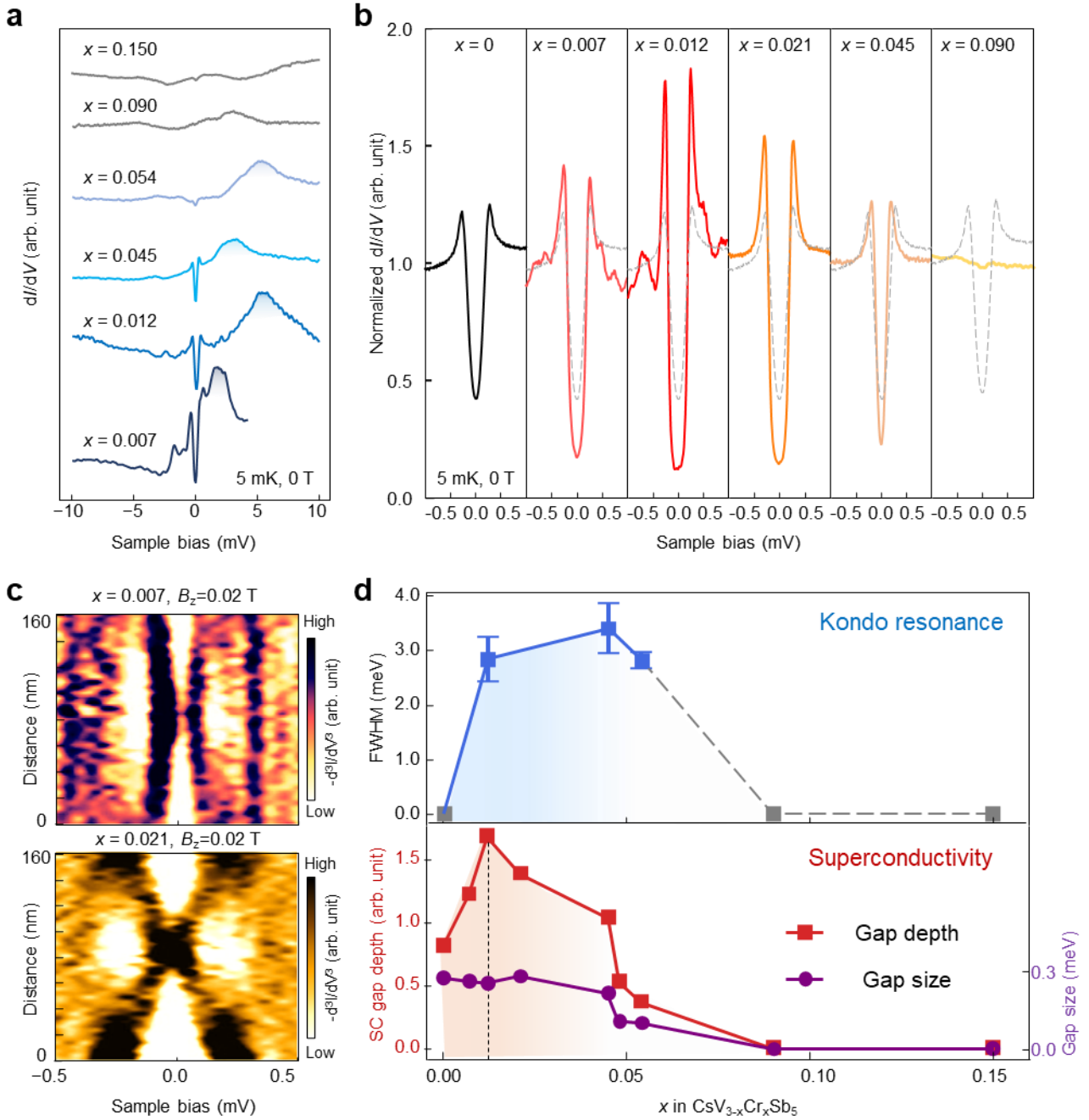


**Fig. 5. Intertwining Kondo resonance with distinct superconductivity in  $\text{CsV}_{3-x}\text{Cr}_x\text{Sb}_5$ .** **a**, Representative  $dI/dV$  spectra of Kondo resonance with Cr concentration  $x = 0.007, 0.012, 0.045, 0.054, 0.09$  and  $0.15$ , respectively. **b**, Evolution of spatially averaged  $dI/dV$  spectra with different Cr concentrations ( $V_s = -5$  mV,  $I_t = 1$  nA,  $V_{\text{mod}} = 10$   $\mu\text{V}$ ,  $T_{\text{base}} = 5$  mK). **c**, Second-derivative plot of the  $dI/dV$  linecut across the vortex core in sample with  $x = 0.007$  and  $x = 0.021$ , showing distinct spatial evolution of vortex bound states. **d**, Evolution of Kondo resonance peak width (up) and superconducting gap size  $\Delta$  (down) with Cr concentrations  $x$ , show strong correlation between Kondo effect and superconductivity. The FWHM of Kondo resonance in each concentration are determined by fitting with Frota function.

The Kondo resonances are observed on all slightly doped sample (Supplementary Fig. 4). With increasing concentrations  $x$  of Cr, the resonance peak of representative Kondo resonance gradually becomes broader and lower (Fig. 5a). When  $x$  increases to 0.09, the Kondo resonance is indistinguishable in the low-energy  $dI/dV$  spectra (Supplementary Fig. 8). The suppression of Kondo effect with increasing Cr concentrations indicates that strong Ruderman–Kittel–Kasuya–Yosida (RKKY) interactions between Cr dopants would lead to spin-glass behavior and modifications to the Kondo effect from impurity-impurity spin interactions<sup>40,42</sup>.

Meanwhile, the superconductivity shows intriguing evolution with Cr concentrations as indicated by the spatially averaged  $dI/dV$  spectra at a low temperature of 5 mK (Fig. 5b). In pristine sample, the superconducting gap show V-shaped pairing gap with residual in-gap states<sup>12</sup>. In the slightly doped sample, the peak-to-peak SC gap size  $\Delta$  does not intensively change. However, the coherence peak height at the gap edge  $P=dI/dV(E=\Delta)$  and SC gap depth  $H=P-dI/dV(E=0)$  show different evolution with  $x$ . Both  $P$  and  $H$  become higher with increasing  $x$  and reaches maximum at  $x = 0.012$ .

The enhanced coherence peak and SC gap depth indicates higher superfluid density<sup>43</sup>. To further characterize the exotic superconductivity with enhanced gap depth, we apply vertical magnetic fields to the samples with  $x = 0.007$  and  $0.021$  to investigate possible differences of Abrikosov vortices. By applying 20 mT magnetic field, hexagonal vortex lattice form in both samples (Supplementary Fig. 9). However,  $dI/dV$  linecut measured across vortex and corresponding second-derivative  $d^3I/dV^3$  spectra have shown different characteristic for these two different samples. For  $x = 0.007$ , an X-shaped spatial evolution of vortex bound state (VBS) is observed (Fig. 5c), been the same with well-studied pristine  $\text{CsV}_3\text{Sb}_5$ . For  $x = 0.021$ , a non-splitting Y-shaped spatial evolution of VBS is observed (Fig. 5c), different with pristine  $\text{CsV}_3\text{Sb}_5$  and  $\text{CsV}_{3-x}\text{Cr}_x\text{Sb}_5$  with  $x = 0.007$ . The change of the VBS behavior when increasing Cr concentrations from 0 to 0.021 can be regard as a possible phase transition, further supporting the existence of a distinct phase<sup>44</sup>.

The phase diagram of Kondo effect and superconductivity with Cr concentrations show the strong interplay of superconductivity with Kondo resonance (Fig. 5d). Coinciding with the observations of Kondo effect, the superconducting gap size keeps nearly unchanged but the gap depth shows a dome like evolution. The gap size is not suppressed by the local moment due to the Kondo screening by the itinerant electrons when the Kondo temperature  $T_K$  is higher than  $T_c$ . The dominant role of Cr dopants is the electron doping which may result in the dome-like evolution of gap depth. The enhancement of gap depth indicates a distinct superconductivity phase. Following the disappearance of Kondo effect, both gap size and depth suddenly drop when  $x > 0.05$ . With Cr concentrations further increase, the RKKY interactions induced local magnetic ordering evolves, which results in the suppression of both superconductivity<sup>24-26</sup> and Kondo effect<sup>27,45</sup>.

In conclusion, we explore the interplay between local magnetic moments and superconductivity in Cr-doped kagome superconductor  $\text{CsV}_{3-x}\text{Cr}_x\text{Sb}_5$ . We demonstrate that Cr doping induces Kondo resonances near the Fermi level, which propagate anisotropically, breaking local mirror symmetries. The observed anisotropic Kondo resonance is attributed to the antiferromagnetic coupling between

itinerant electrons and the spin-up electrons induced by Cr-dopant moments, driven by magnetic frustration in the kagome lattice. This interaction enhances superconductivity in the low-doping regime, leading to a significant increase in the coherence peak height and superconducting gap depth. Furthermore, we observe unconventional spatial evolution of vortex bound states in the Kondo resonance phase, which is suppressed as magnetic ordering emerges. Our findings reveal a distinct superconducting phase in  $\text{CsV}_{3-x}\text{Cr}_x\text{Sb}_5$ , providing new insights into the coupling between superconductivity and magnetism in kagome systems, and opening new avenues for the study of unconventional superconductivity in these materials.

## References

- 1 Stewart, G. R. Unconventional superconductivity. *Advances in Physics* **66**, 75-196 (2017).
- 2 Scalapino, D. J. A common thread: The pairing interaction for unconventional superconductors. *Reviews of Modern Physics* **84**, 1383-1417 (2012).
- 3 Ran, S. *et al.* Nearly ferromagnetic spin-triplet superconductivity. *Science* **365**, 684-687 (2019).
- 4 Ortiz, B. R. *et al.* New kagome prototype materials: discovery of  $KV_3Sb_5$ ,  $RbV_3Sb_5$ , and  $CsV_3Sb_5$ . *Physical Review Materials* **3**, 094407 (2019).
- 5 Ortiz, B. R. *et al.*  $CsV_3Sb_5$ : A Z2 Topological Kagome Metal with a Superconducting Ground State. *Physical Review Letters* **125**, 247002 (2020).
- 6 Guo, H. M. & Franz, M. Topological insulator on the kagome lattice. *Physical Review B* **80**, 113102 (2009).
- 7 Tang, E., Mei, J. W. & Wen, X. G. High-Temperature Fractional Quantum Hall States. *Physical Review Letters* **106**, 236802 (2011).
- 8 Kiesel, M. L., Platt, C. & Thomale, R. Unconventional Fermi Surface Instabilities in the Kagome Hubbard Model. *Physical Review Letters* **110**, 126405 (2013).
- 9 Xing, Y. Q. *et al.* Localized spin-orbit polaron in magnetic Weyl semimetal  $Co_3Sn_2S_2$ . *Nature Communications* **11**, 5613 (2020).
- 10 Tan, H. X., Liu, Y. Z., Wang, Z. Q. & Yan, B. H. Charge Density Waves and Electronic Properties of Superconducting Kagome Metals. *Physical Review Letters* **127**, 046401 (2021).
- 11 Yang, S.-Y. *et al.* Giant, unconventional anomalous Hall effect in the metallic frustrated magnet candidate,  $KV_3Sb_5$ . *Science Advances* **6**, eabb6003 (2020).
- 12 Chen, H. *et al.* Roton pair density wave in a strong-coupling kagome superconductor. *Nature* **599**, 222-228 (2021).
- 13 Yan, X.-Y. *et al.* Chiral pair density waves with residual Fermi arcs in  $RbV_3Sb_5$ . *arXiv e-prints*, arXiv:2408.03352 (2024).
- 14 Deng, H. *et al.* Chiral kagome superconductivity modulations with residual Fermi arcs in  $KV_3Sb_5$  and  $CsV_3Sb_5$ . *arXiv*, arXiv:2408.02896 (2024).
- 15 Nie, L. P. *et al.* Charge-density-wave-driven electronic nematicity in a kagome superconductor. *Nature* **604**, 59-64 (2022).
- 16 Li, H. *et al.* Unidirectional coherent quasiparticles in the high-temperature rotational symmetry broken phase of  $AV_3Sb_5$  kagome superconductors. *Nature Physics* **19**, 637-643 (2023).
- 17 Wu, P. *et al.* Unidirectional electron-phonon coupling in the nematic state of a kagome superconductor. *Nature Physics* **19**, 1143-1149 (2023).
- 18 Xu, H. S. *et al.* Multiband Superconductivity with Sign-Preserving Order Parameter in Kagome Superconductor  $CsV_3Sb_5$ . *Physical Review Letters* **127**, 187004 (2021).
- 19 Wang, Q. *et al.* Charge Density Wave Orders and Enhanced Superconductivity under Pressure in the Kagome Metal  $CsV_3Sb_5$ . *Advanced Materials* **33**, 2102813 (2021).
- 20 Yang, H. *et al.* Titanium doped kagome superconductor  $CsV_{3-x}Ti_xSb_5$  and two distinct phases. *Science Bulletin* **67**, 2176-2185 (2022).
- 21 Oey, Y. M. *et al.* Fermi level tuning and double-dome superconductivity in the kagome metal  $CsV_3Sb_{5-x}Sn_x$ . *Physical Review Materials* **6**, L041801 (2022).
- 22 Zhong, Y. *et al.* Nodeless electron pairing in  $CsV_3Sb_5$ -derived kagome superconductors. *Nature* **617**, 488-492 (2023).
- 23 Luo, Y. *et al.* A unique van Hove singularity in kagome superconductor  $CsV_{3-x}Ta_xSb_5$  with enhanced superconductivity. *Nature Communications* **14**, 3819 (2023).
- 24 Ding, G., Wo, H., Gu, Y., Gu, Y. & Zhao, J. Effect of chromium doping on superconductivity and charge density wave order in the kagome metal  $Cs(V_{1-x}Cr_x)_3Sb_5$ . *Physical Review B* **106**, 235151 (2022).

- 25 Suzuki, S. *et al.* Evolution of band structure in the kagome superconductor  $\text{Cs}(\text{V}_{1-x}\text{Cr}_x)_3\text{Sb}_5$  Toward universal understanding of charge density wave and superconducting phase diagrams. *Physical Review B* **110**, 165104 (2024).
- 26 Yousuf, S. *et al.* Synthesis and physical properties of Cr-doped Kagome superconductor  $\text{CsV}_3\text{Sb}_5$ . *Current Applied Physics* **61**, 7-11 (2024).
- 27 Capa Salinas, A. N. *et al.* Electron-hole asymmetry in the phase diagram of carrier-tuned  $\text{CsV}_3\text{Sb}_5$ . *Frontiers in Electronic Materials* **3**, 1-7 (2023).
- 28 Guo, Y. *et al.* Ubiquitous Flat Bands in a Cr-based Kagome Superconductor. *arXiv e-prints*, arXiv:2406.05293 (2024).
- 29 Peng, S. *et al.* Flat bands and distinct density wave orders in correlated Kagome superconductor  $\text{CsCr}_3\text{Sb}_5$ . *arXiv e-prints*, arXiv:2406.17769 (2024).
- 30 Liu, Y. *et al.* Superconductivity under pressure in a chromium-based kagome metal. *Nature* **632**, 1032-1037 (2024).
- 31 Wu, S. *et al.* Flat-band enhanced antiferromagnetic fluctuations and superconductivity in pressurized  $\text{CsCr}_3\text{Sb}_5$ . *Nature Communications* **16**, 1375 (2025).
- 32 Zhao, H. *et al.* Cascade of correlated electron states in the kagome superconductor  $\text{CsV}_3\text{Sb}_5$ . *Nature* **599**, 216-221 (2021).
- 33 Kondo, J. Resistance minimum in dilute magnetic alloys. *Progress of Theoretical Physics* **32**, 37 (1964).
- 34 Ternes, M. Probing magnetic excitations and correlations in single and coupled spin systems with scanning tunneling spectroscopy. *Progress in Surface Science* **92**, 83-115 (2017).
- 35 Zhang, Y.-h. *et al.* Temperature and magnetic field dependence of a Kondo system in the weak coupling regime. *Nature Communications* **4**, 2110 (2013).
- 36 Frota, H. O. Shape of the Kondo resonance. *Physical Review B* **45**, 1096-1099 (1992).
- 37 Frota, H. O. & Oliveira, L. N. Photoemission spectroscopy for the spin-degenerate anderson model. *Physical Review B* **33**, 7871-7874 (1986).
- 38 Costi, T. A. Kondo Effect in a Magnetic Field and the Magnetoresistivity of Kondo Alloys. *Physical Review Letters* **85**, 1504-1507 (2000).
- 39 Moore, J. E. & Wen, X.-G. Anomalous Magnetic Splitting of the Kondo Resonance. *Physical Review Letters* **85**, 1722-1725 (2000).
- 40 Kumar, N. *et al.* Atomic-scale magnetic doping of monolayer stanene by revealing Kondo effect from self-assembled Fe spin entities. *Npj Quantum Materials* **9**, 37 (2024).
- 41 Schneider, M. A., Vitali, L., Knorr, N. & Kern, K. Observing the scattering phase shift of isolated Kondo impurities at surfaces. *Physical Review B* **65**, 121406 (2002).
- 42 Boucaï, E., Lecoanet, B., Pilon, J., Tholence, J. L. & Tournier, R. Interaction Effects between Nearly Magnetic Cobalt Impurities in Gold. *Physical Review B* **3**, 3834-3846 (1971).
- 43 Ruan, W. *et al.* Visualization of the periodic modulation of Cooper pairing in a cuprate superconductor. *Nature Physics* **14**, 1178-1182 (2018).
- 44 Huang, Z. *et al.* Tunable vortex bound states in multiband  $\text{CsV}_3\text{Sb}_5$ -derived kagome superconductors. *Science Bulletin* **69**, 885-892 (2024).
- 45 Maple, M. B. Superconductivity - probe of magnetic state of local moments in metals. *Applied Physics* **9**, 179-204 (1976).
- 46 Perdew, J. P., Burke, K. & Ernzerhof, M. Generalized Gradient Approximation Made Simple. *Physical Review Letters* **77**, 3865-3868 (1996).
- 47 Blöchl, P. E. Projector augmented-wave method. *Physical Review B* **50**, 17953-17979 (1994).
- 48 Kresse, G. & Furthmüller, J. Efficient iterative schemes for ab initio total-energy calculations using a plane-wave basis set. *Physical Review B* **54**, 11169-11186 (1996).

- 49 Grimme, S., Antony, J., Ehrlich, S. & Krieg, H. A consistent and accurate ab initio parametrization of density functional dispersion correction (DFT-D) for the 94 elements H-Pu. *The Journal of Chemical Physics* **132**, 154104–154123 (2010).
- 50 Neugebauer, J. & Scheffler, M. Adsorbate-substrate and adsorbate-adsorbate interactions of Na and K adlayers on Al(111). *Physical Review B* **46**, 16067-16080 (1992).
- 51 Tersoff, J. & Hamann, D. R. Theory and Application for the Scanning Tunneling Microscope. *Physical Review Letters* **50**, 1998-2001 (1983).

## Methods

**Single crystal growth of CsV<sub>3-x</sub>Cr<sub>x</sub>Sb<sub>5</sub>.** Single crystals of CsV<sub>3-x</sub>Cr<sub>x</sub>Sb<sub>5</sub> were grown via a modified self-flux method<sup>12,20</sup>.

**Scanning tunneling microscopy/spectroscopy.** The samples used in the STM/S experiments were cleaved at low temperature (10 K) and immediately transferred to an STM chamber and cooled down to 4.2 K. Experiments were performed in an ultrahigh vacuum ( $1 \times 10^{-10}$  mbar) ultra-low temperature STM system equipped with external magnetic field perpendicular to the sample surface. The lowest base temperature is 5 mK with an electronic temperature of 138 mK (calibrated using a standard superconductor, Al crystal). The magnetic field was applied using the zero-field cooling technique. All the scanning parameters (setpoint voltage  $V_s$  and tunneling current  $I_t$ ) of the STM topographic images are listed in the figure captions. The  $dI/dV$  spectra were acquired by a standard lock-in amplifier at a modulation frequency of 973.1 Hz, the modulation bias ( $V_{\text{mod}}$ ) is listed in the figure captions. Non-magnetic tungsten tips were fabricated via electrochemical etching and calibrated on a clean Au(111) surface prepared by repeated cycles of sputtering with argon ions and annealing at 500 °C.

**Identification of Cr concentrations.** The diluted Cr concentrations are determined microscopically by counting numbers of dumbbell-like protrusions with high accurate in the STM images of Sb terminated surfaces (Fig. 1b-d). With Cr concentrations further increasing to  $x > 0.054$ , it is difficult to discern the number of dumbbell-like protrusions in the STM images (Fig. 1e-g) and therefore the concentrations are verified macroscopically by Energy-Dispersive X-ray Spectroscopy (EDS).

**Density functional theory calculations.** Our density functional theory (DFT) calculations were carried out using the generalized gradient approximation (GGA) for the exchange correlation potential in the form of PerdewBurke–Ernzerhof (PBE)<sup>46</sup>, the projector augmented wave method<sup>47</sup>, and a plane-wave basis set as implemented in the Vienna ab-initio simulation package (VASP)<sup>48</sup>. We also included the dispersion correction through Grimme’s semiempirical D3 scheme<sup>49</sup> in combination with the PBE functional (PBE-D3). A kinetic energy cutoff of 350 eV for the planewave basis was adopted for structural relaxations and electronic structure calculations. A  $6 \times 6 \times 2$  asymmetric slab model was employed in our calculations. A vacuum layer of 20 Å in thickness was employed to reduce imaging interactions between adjacent supercells. Dipole correction was considered in all calculations to correct the error introduced by the periodic boundary condition and balance the vacuum level differences on the different sides of the polarized surfaces<sup>50</sup>. The lowest layer of the CsV<sub>3</sub>Sb<sub>5</sub> slab was fixed, while the remaining layers were allowed to relax until the residual force per atom was below 0.01 eV/Å. In the topmost layer, one vanadium (V) atom was replaced by a chromium (Cr) atom to model the substitution of V by Cr. A Gamma-only  $k$ -mesh was used to sample the Brillouin zone of the super cell. The Methfessel-Paxton method with a  $\sigma$  value of 0.05 eV was applied for structural relaxation and electronic structure calculations. The STM images were calculated using the Tersoff-Hamann method<sup>51</sup>.

**Acknowledgements:** We thank Dr. Zhan Wang for helpful discussions. The work is supported by grants from the National Natural Science Foundation of China (62488201, 92477205), the National Key Research and Development Projects of China (2022YFA1204100, 2023YFA1406500), the CAS Project for Young Scientists in Basic Research (YSBR-003) and the Innovation Program of Quantum Science and Technology (2021ZD0302700). Z.W. is supported by the US DOE, Basic Energy Sciences (Grant No. DE-FG02-99ER45747) and by Research Corporation for Science Advancement (Cottrell SEED award number 27856). Calculations were performed at the Hefei Advanced Computing Center, the Physics Lab of High-Performance Computing (PLHPC) and the Public Computing Cloud (PCC) of Renmin University of China.

**Author Contributions:** H.-J. G. and H. C. design the experiments. Z.H., H.C. and H.Z. performed the STM/S experiments and data analysis with the technical assistant from C.S.. Z.Zhao. and H.Y. prepared the CsV<sub>3</sub>Sb<sub>5</sub> samples. Z.W. did the theoretical consideration. Z.Zhang and W.J. carried out theoretical calculations and analysis. Z.H., H.C., Z.Zhang, W.J. and H.-J.G. wrote the manuscript with input from all other authors. H.-J.G. supervised the project.

**Competing Interests:** The authors declare that they have no competing interests.